Journal of Materials Chemistry A

PAPER

View Article Online
View Journal

Cite this: DOI: 10.1039/c7ta08400e

Aligned and stable metallic MoS_2 on plasma-treated mass transfer channels for the hydrogen evolution reaction†

Lei Yang,[a] Alolika Mukhopadhyay,[a] Yucong Jiao,[a] Jonathan Hamel,[a] Mourad Benamara,[b] Yingjie Xing[a] and Hongli Zhu *[a]

Ultra-thin molybdenum disulfide (MoS_2) nanosheets have attracted intensive attention due to their catalytic properties. However, most of the previously described MoS_2 nanosheets show poor electrical conductivity and a limited amount of active sites. Moreover, these nanosheets tend to restack severely due to van der Waals forces causing a reduction in the density of their active sites. Inspired by nature, for the first time, we have vertically grown 1T metallic MoS_2 on well-aligned, freestanding, 1000 μm long channels obtained from carbonized wood to maximize the exposition of active catalytic sites and increase the electrolyte and hydrogen transport through the well-aligned channels using a scalable approach. Furthermore, the carbonized wood surface was plasma treated to assist the dissipation of generated hydrogen, thus reducing the proton transport barrier at the electrode surface. The vertically grown 1T metallic MoS_2 on thoroughly aligned long carbonized wood channels exhibits remarkable catalytic activity with an operating overpotential of 128 mV at a current density of 10 mA cm^{-2}. This work provides a new approach for 1T metallic MoS_2 synthesis and an interesting configuration to optimize and maintain the active catalytic sites and dissipate hydrogen on time by *in situ* vertically grown catalyst on the well-aligned channels made by nature.

Received 22nd September 2017
Accepted 10th November 2017

DOI: 10.1039/c7ta08400e

rsc.li/materials-a

Introduction

Hydrogen (H_2) is considered as one of the most environmentally friendly energy carriers to replace traditional non-renewable fossil fuels.[1,2] Although platinum (Pt) is the most efficient electrocatalyst used to improve the kinetics and efficiency of the hydrogen evolution reaction (HER), the cost of Pt is extremely high. Several economical materials have been extensively investigated for high-performance HER to replace the expensive and scarce Pt, such as transition metals chalcogenides,[3,4] non-noble metal alloys,[5] phosphides,[6] nitrides[7] and carbides.[8] Among these electrocatalysts, two-dimensional (2D) molybdenum disulfide (MoS_2) has demonstrated excellent catalytic activity for H_2 production due to its ample active sites located at the crystal edges.[9] However, the HER activity of MoS_2 is traditionally lower than that of Pt and it is important to improve the activity of MoS_2 for practical applications. MoS_2 has two phases: a metallic 1T phase and a semiconducting 2H phase. Previous studies have found that the basal plane of the semiconducting 2H phase MoS_2 is catalytically inert for the HER, whereas the basal planes of metallic 1T MoS_2 are rich in active sites.[10,11] Meanwhile, compared to the 2H phase MoS_2,[12] the 1T phase MoS_2 has superior electron transfer capability due to its 5–7 fold higher electrical conductivity, which has the benefits of higher reaction kinetics for the electrons and protons (H^+) on the active sites.[13]

However, the 1T phase MoS_2 is in a metastable state and due to its instability, the existence of 1T MoS_2 in nature is rare.[10] Furthermore, the 1T phase MoS_2 tends to rapidly restack and transform to the 2H phase MoS_2 due to the S–S van der Waals forces.[12,14] Consequently, this will significantly reduce the density of its active sites and the ability to transfer electrons, which inhibits the HER performance. Most previous studies have used MoS_2 laminated glassy carbon as the working electrode to carry out HER studies,[15,16] however, the aggregation of MoS_2 on the glassy carbon significantly decreases the density of its active sites.[17] Therefore, freestanding structures have been investigated to overcome the abovementioned drawbacks, such as the vertical growth of MoS_2 on conductive substrates[18–20] and the fabrication of freestanding MoS_2 films.[21,22] Xiang *et al.*[23] reported that the double layer capacitance (C_{dl}) of a 2H MoS_2 nanosheet array on carbon cloth (9 mF) has 4.5 times higher than the C_{dl} found for pure 2H MoS_2 (2 mF), which contributes to its outstanding performance in the HER. However, all the substrates studied in the literature are composed of randomly

[a]Department of Mechanical and Industrial Engineering, Northeastern University, Boston, Massachusetts 02115, USA. E-mail: h.zhu@neu.edu

[b]Institute for Nanoscale Materials Science and Engineering, University of Arkansas, Fayetteville, Arkansas 72701, USA

† Electronic supplementary information (ESI) available. See DOI: 10.1039/c7ta08400e

distributed building blocks. For example, carbon cloth is composed of disordered and layer-by-layer overlapped carbon fibers, which severely increase the flow resistance of the electrolyte and H_2 transportation.[20]

Wood is composed of well-aligned channels in the growth direction that assist in the metabolic transfer of water and nutrients. These well-aligned channels retain their cohesive structure even after carbonization. Herein, for the first time, we have utilized the well-aligned carbonized wood channels as a substrate to support the *in situ* vertical growth of 1T MoS_2 as a catalyst for H_2 production. The well-aligned wood channels not only provide a base for MoS_2 growth but also provide channels for H^+ transport and H_2 dissipation. Because of the vertical growth configuration of the catalyst, compared to the 1T MoS_2 coated glassy carbon substrate, the C_{dl} of the freestanding carbonized wood/1T MoS_2 (termed as CW/1T MoS_2) increased approximately 3.5 fold from 11 mF to 38 mF, which drastically escalates the effective active surface sites in the HER while maintaining its stability.

Due to the inadequate water affinity of rotating disk electrodes (RDE), the formation and agglomeration of H_2 bubbles on conventional electrode surfaces is a barrier for the HER, which can passively influence electrolyte transport[24] and further block the catalytic active sites.[25] Very few studies have been conducted to solve this problem. In our study, an anisotropic plasma treatment was further conducted to improve the hydrophilicity of the carbonized wood substrate with well-aligned channels in order to improve aqueous electrolyte transport and H_2 bubble emission.

The hierarchal configuration of 1T MoS_2 vertically grown on the well-aligned and hydrophilic channels has the following advantages: (1) maximizing the exposure of the active sites in the edges and basal plane of 1T metallic MoS_2 and enhancing its performance in the HER, (2) minimizing the restacking of the 2D nanosheets, (3) removing the barrier layer of large H_2 bubbles, assisting the exhaustion of H_2 and subsequently maintaining favorable reaction kinetics, and (4) benefiting electrolyte and H^+ transfer. CW/1T MoS_2 exhibits promising catalytic activity with operating overpotentials as low as 128 mV at a current density of 10 mA cm^{-2}. After 1000 cycles of continuous operation, CW/1T MoS_2 exhibits a decay of only 6.3% in its electrocatalytic current density.

Results and discussion

Freestanding carbonized wood with one uniform layer of 1T MoS_2 grown on the surface of the well-aligned channels can be, in principal, beneficial as an electrocatalytic electrode used for the HER. As illustrated in the Fig. 1(a), the vertical 1T MoS_2 nanosheets act as the catalyst by exposing the maximum

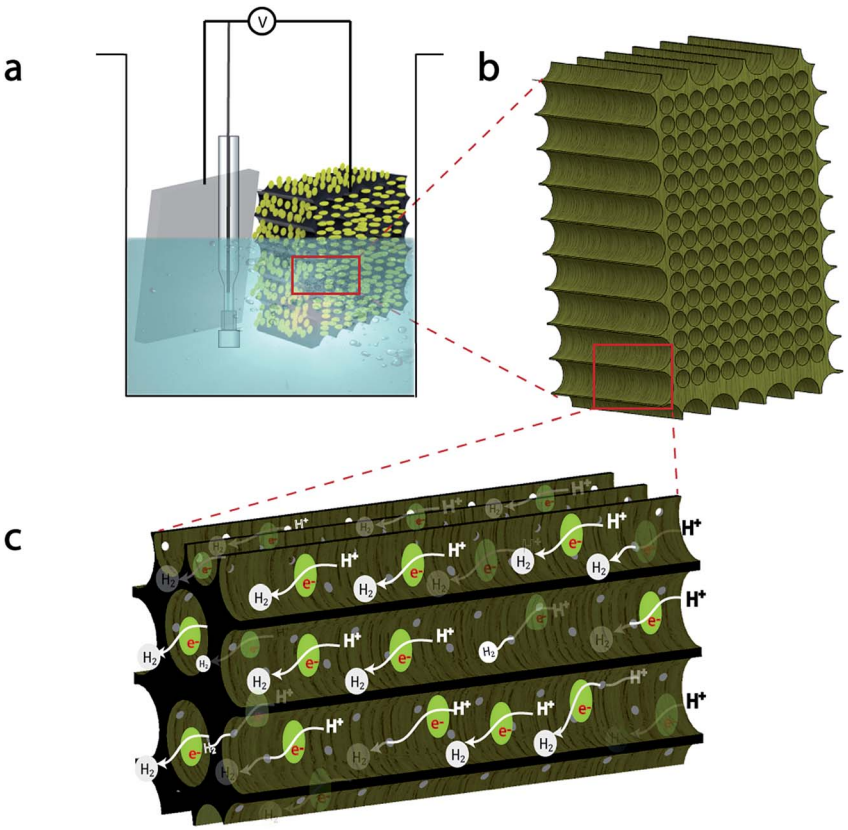

Fig. 1 A schematic of (a) the setup used for the HER tests using freestanding CW/1T MoS_2 as the working electrode, platinum foil as the counter electrode and Ag/AgCl as the reference electrode, (b) the 1T MoS_2 uniformly grown on the long and well-aligned carbonized wood channels and (c) the catalytic mechanism of H^+ reduction to H_2 molecules in the 1T MoS_2 vertically grown on the well-aligned channels of carbonized wood.

attainable number of active sites. The open and aligned channels provide readily accessible and efficient H^+ transport and the conductive carbonized wood substance provides rapid electron transport and H_2 bubble release pathways. ESI Video 1† vividly shows the H_2 bubbles are easily separated from the surface of the freestanding working electrode comprised of CW/1T MoS_2. When compared to CW/1T MoS_2, the ESI Video 2† of 1T MoS_2 deposited on glassy carbon shows that the H_2 bubbles are severely agglomerated, even if the rotation speed is quite high. Fig. 1(b) depicts the long and well-aligned channels covered with one uniform layer of 1T MoS_2 on the freestanding carbonized wood electrode. The highly active sites and excellent mass transfer contribute to the higher HER performance with the synergistic effects of the well-aligned channels in the carbonized wood substrate and the vertical growth of the 1T MoS_2. As demonstrated in Fig. 1(c), the electrons approaching the active sites of the 1T MoS_2 nanosheet direct react with H^+ in the electrolyte to form H_2. The emission of H_2 bubbles accelerates the flow of the electrolyte, successively supplying the channels with fresh electrolyte, which further increases the contact probability between the electrons and H^+. In addition, numerous pit holes exist on the wall between the neighboring channels, which are presented as a grey color in Fig. 1(c) and also proliferate electrolyte transfer between the adjacent channels.

Wood, as an abundant, renewable and freestanding material, is used extensively in daily life. In nature, the aligned channel structures of wood evolve in the direction of growth in order to satisfy the needs of nutrient and water transport (Fig. 2(a)). In this research, the high-temperature carbonization of natural wood in an argon environment was executed to prepare the inexpensive conductive carbon with well-aligned channels. The evenly distributed channel structure of wood can withstand very high-temperature annealing and uphold its structural integrity, as shown in Fig. 2(b). In our work, we performed a plasma treatment to improve the hydrophilicity of the carbonized wood. The improved hydrophilicity of the plasma treated carbonized wood (ESI Video †) significantly improved electrolyte transport and H_2 bubble emission. Another advantage of the channel architecture is that the carbonized wood

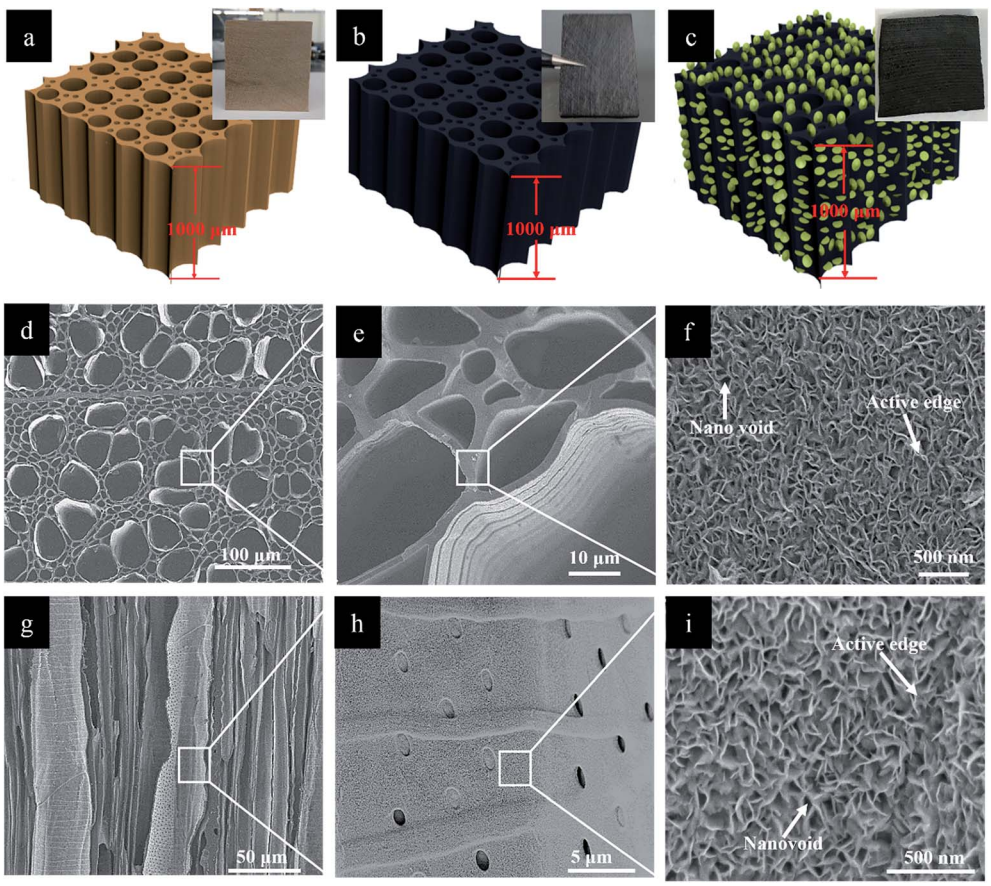

Fig. 2 A schematic of (a) the wood channels along the axial direction from a tree trunk; the inset shows a digital image of the wood, (b) the wood channels along the axial direction after the carbonization process; the inset shows a digital photograph of the carbonized wood, and (c) the CW/1T MoS_2 in the axial direction after the growth of 1T MoS_2; the inset shows a digital photograph of the freestanding CW/1T MoS_2. (d and e) Top-view SEM images of the transverse cross-section of 1T MoS_2 grown on the carbonized wood channels at different resolutions. (f) A magnified top-view SEM image indicating the unique morphology of the MoS_2 vertical array on the surface of carbonized wood. (g) SEM images of a longitudinal cross-section of the carbonized wood showing the well-aligned channels. (h) A magnified image of the interior morphology of the well-aligned channels after MoS_2 growth. (i) A SEM image clearly showing the distinguishable morphology of the MoS_2 perpendicular array on the surface of the channel walls.

allows the MoS_2 precursor to effortlessly access the channels and thereafter, result in an exceptionally high surface area for 1T MoS_2 growth. Fig. 2(c) and S1† show the conformity of the 1T MoS_2 vertically grown on the long and well-aligned channels of carbonized wood (1000 μm thick). The morphology of a transverse section of the CW/1T MoS_2 was characterized using a scanning electron microscopy (SEM). These SEM images are shown in Fig. 2(d–f). In Fig. 2(d and e), it is clear that the channel structure was retained after the growth of the 1T MoS_2 nanosheets, which ensures the efficient diffusion of the electrolyte and the emission of H_2 gas. The high magnification SEM image (Fig. 2(f)) shows that growing the 1T MoS_2 nanosheets uniformly and vertically on the carbonized wood surface maximizes the exposure of the edge and basal plane active sites. Also, the morphology of the longitudinally cut section explicitly shows the successful growth of 1T MoS_2 inside the carbonized wood channels (Fig. 2(g–i)). Fig. 2(g) shows a typical low-magnification SEM image of the well-aligned channels. Pit holes with a diameter of approximately 1 μm were observed on the channel walls in Fig. 2(h) and were expected to facilitate electrolyte transport between the adjacent channels. The magnified image in Fig. 2(i) reveals the organization of 1T MoS_2 into a perpendicular array in the channel walls and the channel surface being completely covered by the vertically grown 1T MoS_2 nanosheets. The 1T MoS_2 nanosheets were immobilized in the carbonized wood, which prevents the aggregation of 1T MoS_2 and greatly stabilized the active sites for a long period. The nano-voids, as shown in the Fig. 2(f and i), between the adjacent 1T MoS_2 nanosheets are expected to expose the basal plane active sites and enhance the HER performance by promoting the diffusion of the electrolyte.

High-resolution transmission electron microscopy (HRTEM) was performed to examine the microstructure and crystallinity of CW/1T MoS_2. The ultra-thin 1T MoS_2 nanosheets display distinct ripples and corrugation in the low-magnification TEM images, as shown in Fig. 3(a). Fig. 3(b) prominently display the differences between carbonized wood and 1T MoS_2. The 1T MoS_2 counterpart exhibits the edge of the layers of the 2D nanosheets in the white line area of Fig. 3(b). The carbonized wood exhibits a short-range ordered pattern and amorphous structure, as shown in Fig. S2.† The regular layer structure and curled edges of the 1T MoS_2 nanosheets are displayed in the HRTEM images, as presented in Fig. S3.† The high-magnification HRTEM image shows few layered MoS_2 with an interlayer distance of 6.4–6.5 Å (Fig. 3(c)). The selected area electron diffraction (SAED) patterns of the 1T MoS_2 nanosheets exhibit hazy and broad diffraction rings, which indicates the low crystallization of 1T MoS_2 after its vertical growth on the surface of the carbonized wood (Fig. 3(d)).[26]

Raman and X-Ray Diffraction (XRD) spectra were collected to confirm the carbonization of wood and growth of 1T MoS_2. In the Raman spectra (Fig. 4(a), bottom black curve), strong Raman shifts were observed at 149, 235 and 334 cm^{-1}, which are the characteristic peaks of the phonon mode in 1T MoS_2.[27] Similar Raman peaks in the CW/1T MoS_2 sample provide important evidence for the formation of the metallic phase

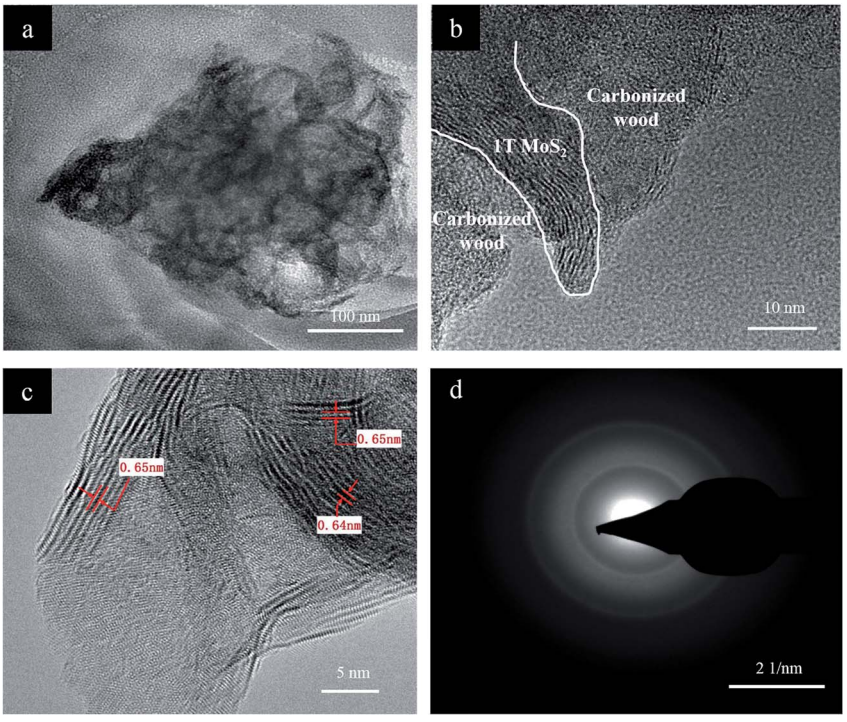

Fig. 3 (a) The low-magnification TEM image of the 1T MoS_2 nanosheets vertically grown on carbonized wood. (b) The HRTEM image of the various regions of the carbonized wood and 1T MoS_2 nanosheets. The 1T MoS_2 region is labeled with the white line. (c) The high-magnification HRTEM image of the carbonized wood and 1T MoS_2 nanosheets. The interlayer distance of the 1T MoS_2 nanosheets was 6.4–6.5 Å. (d) The SAED pattern of the 1T MoS_2 nanosheets.

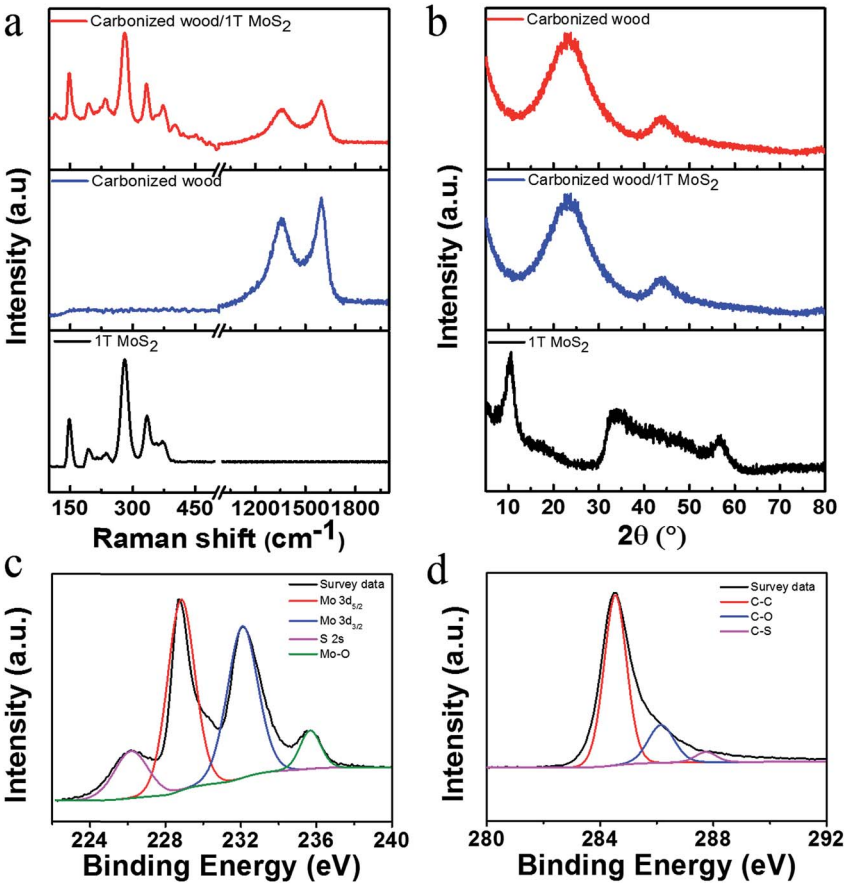

Fig. 4 (a) The Raman spectra of pure 1T MoS_2, carbonized wood and CW/1T MoS_2. (b) XRD of pure 1T MoS_2, carbonized wood and CW/1T MoS_2. (c) The high-resolution XPS spectra of elemental Mo in CW/1T MoS_2. (d) The high-resolution XPS spectra of elemental C in CW/1T MoS_2.

MoS_2 in the carbonized wood substrate, as shown in Fig. 4(a), top red curve. The peaks at 1338 cm^{-1} and 1595 cm^{-1} were attributed to the D and G bands of carbon, respectively, and indicate the complete conversion from pristine wood to carbon in the carbonized wood (Fig. 4(a), middle blue curve). These results prove that the CW/1T MoS_2 sample was composed of carbonized wood and 1T MoS_2. As shown in Fig. 4(b), top and middle curves, two broad diffraction peaks at 23.54° and 43.42° were observed, which are the two respective peaks corresponding to the (002) and (100) planes of carbon in both carbonized wood and the CW/1T MoS_2 samples. The XRD pattern of pure 1T MoS_2 exhibited two characteristic peaks at 10.7° and 17.4°, which correspond to the (002) and (004) reflection of 1T MoS_2, respectively (Fig. 4(b), bottom curve).[28] The asymmetric reflection peak at 33.86° provides evidence of the effect of stacking faults between two S–Mo–S layers due to the intercalation of *N*,*N*-dimethylformamide (DMF), which can improve the HER catalytic activity.[28,29] However, the characteristic peaks of 1T MoS_2 disappeared in the CW/1T MoS_2 sample. This can be caused by an inadequate mass loading of 1T MoS_2 on the carbonized wood substrate. The 1T MoS_2 content in CW/1T MoS_2 was determined using thermogravimetric analysis (TGA) (Fig. S4†). The apparent degradation of 1T MoS_2 appeared in the range of 200–430 °C and was also very profound in the TGA curve obtained for CW/1T MoS_2 as a result of the weight loss of 1T MoS_2. The quantity of 1T MoS_2 in CW/1T MoS_2 was calculated to be 7.10% (Fig. S4†).

The chemical states of elemental Mo and C were investigated by X-ray photoelectron spectroscopy (XPS) after the 1T MoS_2 was vertically grown on the well-aligned carbonized wood channels. In Fig. 4(c), the Mo 3d high-resolution spectrum of MoS_2 displays two characteristic peaks at 228.7 and 231.9 eV, corresponding to the Mo–S bonds. When compared with the XPS spectrum of 1T MoS_2 (Fig. S5†), one new peak emerged at 235.6 eV in CW/1T MoS_2, in accordance with that previously reported, which can be ascribed to the Mo–O bond (as shown in Fig. 4(c)).[30,31] The formation of the Mo–O bond indicated that the hydroxyl (–OH) groups formed due to the plasma treatment of the carbonized wood also participated in the synthesis of MoS_2. Fig. 4(d) shows the two fitted characteristic peaks at 284.8 eV and 286.2 eV, indicative to the C–C and C–O bonds, respectively. The C–O bond was prevalent in the carbonized wood by virtue of the anisotropic plasma treatment, which increases the hydrophilicity of the carbonized wood by introducing hydroxyl moieties onto the carbonized wood surface. In addition, a weak peak also appeared at 287.5 eV, which was attributed to the C–S bonds and is conducive to electron transfer according to Wang's report.[32]

The catalytic activity of the freestanding CW/1T MoS_2 was investigated in a standard three-electrode set-up using a 0.5 M

H_2SO_4 solution as the electrolyte. The polarization curves in Fig. 5(a) shows that CW/1T MoS_2 has a low overpotential of 128 mV *versus* the reversible hydrogen electrode (RHE), which is remarkably lower than that found for 1T MoS_2 drop-coated on a conventional RDE (199 mV *vs.* RHE) at a current density of 10 mA cm^{-2}. The performance of 1T MoS_2 loaded directly on the glassy carbon disk electrode further verified that the number of active sites of 1T MoS_2 was significantly reduced due to nanosheet restacking on the glassy carbon electrode during the drying process. We also found that the emission of H_2 bubbles from the surface of CW/1T MoS_2 was substantially easier and quicker than that of 1T MoS_2 loaded on the RDE, as shown in ESI Video 1 and 2.† The H_2 bubbles cover the surfaces of 1T MoS_2 even at a high rotational speed, which hinders the interaction between the active material and the electrolyte. The HER activity of pure carbonized wood, 2H MoS_2 and carbonized wood/2H MoS_2 (CW/2H MoS_2) were compared with 1T MoS_2. We observed that the pure carbonized wood exhibited hardly any HER activity. 2H MoS_2 and CW/2H MoS_2 have overpotentials of 283 and 177 mV *vs.* RHE, respectively, which are substantially larger than that found for CW/1T MoS_2 at a current density of 10 mA cm^{-2}. To obtain further evidence for the catalytic activity of CW/1T MoS_2, the Tafel slopes of the various catalysts were investigated (Fig. 5(b)). The Tafel slope obtained for CW/1T MoS_2 was 71 mV per decade, which was much lower than that found for 2H MoS_2 (149 mV per decade) and CW/2H MoS_2 (103 mV per decade). Zhang *et al.*[33] have reported that the Tafel slope of MoS_2 nanosheet/Mo_2C-embedded N-doped carbon nanotubes (MoS_2/Mo_2C-NCNTs) was 69 mV per decade, which was similar to our results. The small Tafel slope and overpotential of CW/1T MoS_2 is beneficial for practical H_2 production since the HER performance will increase dramatically as the overpotential decreases.

The electrochemical stability is another critical aspect in evaluating the catalytic activity of a material for HER performance. Similar polarization curves before and after 1000 cycles were demonstrated in Fig. 5(c). The results show that the overpotential at a constant current density of 10 mA cm^{-2} increased by only 8 mV from 128 mV in the first cycle to 136 mV after 1000 cycles. This negligible degeneration (6.3%) confirmed that the active sites of CW/1T MoS_2 are stable in the acidic electrolyte and maintained their freestanding and integral structure after long-term cycling. The SEM and Raman spectra of CW/1T MoS_2 after the HER test also demonstrated the stability of 1T MoS_2 during the HER, as shown in Fig. S6.† Electrochemical impedance spectroscopy (EIS) was used to investigate the HER kinetics of CW/1T MoS_2 (Fig. 5(d)). The Nyquist plots indicate a significant decrease in the charge transfer resistance (R_{ct}) was observed for CW/1T MoS_2 (~4 Ω) when compared to 1T MoS_2 (~11 Ω). Meanwhile, the R_{ct} of 1T MoS_2 was significantly lower than that found for 2H MoS_2 (~33 Ω), which may be induced by the lower conductivity of 2H MoS_2 at the same mass loading (~0.1 mg cm^{-2}). Yu *et al.*[34] also found that the vertical growth of MoS_2 nanosheets arrays on carbonized fiber cloth (CFC) can significantly decrease the R_{ct} of MoS_2/CFC electrocatalysts. The structural characterization and EIS results showed that the vertical growth of 1T MoS_2 nanosheets on carbonized wood used as the working electrode was a prevailing aspect in enhancing the catalytic activity of 1T MoS_2.

Fig. S7(a)† shows the 2H MoS_2 was obviously aggregated, which may be the main reason for the low HER activity of 2H MoS_2 due to the exposure of fewer active edges on the glassy

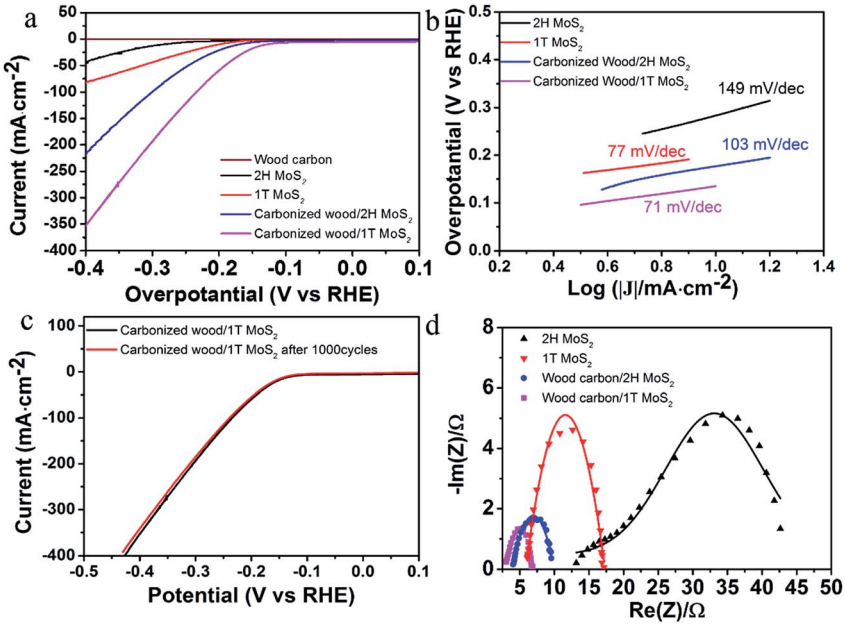

Fig. 5 (a) The polarization curves obtained for carbonized wood, 1T MoS_2, 2H MoS_2, CW/1T MoS_2 and CW/2H MoS_2 at a scan rate of 2 mV s^{-1}. (b) The Tafel plots obtained for 1T MoS_2, 2H MoS_2, CW/1T MoS_2 and CW/2H MoS_2 in the linear region. (c) The electrochemical stability of CW/1T MoS_2 at a scan rate of 2 mV s^{-1} after 1000 continuous cycles. (d) The Nyquist plots obtained for 1T MoS_2, 2H MoS_2, CW/1T MoS_2 and CW/2H MoS_2.

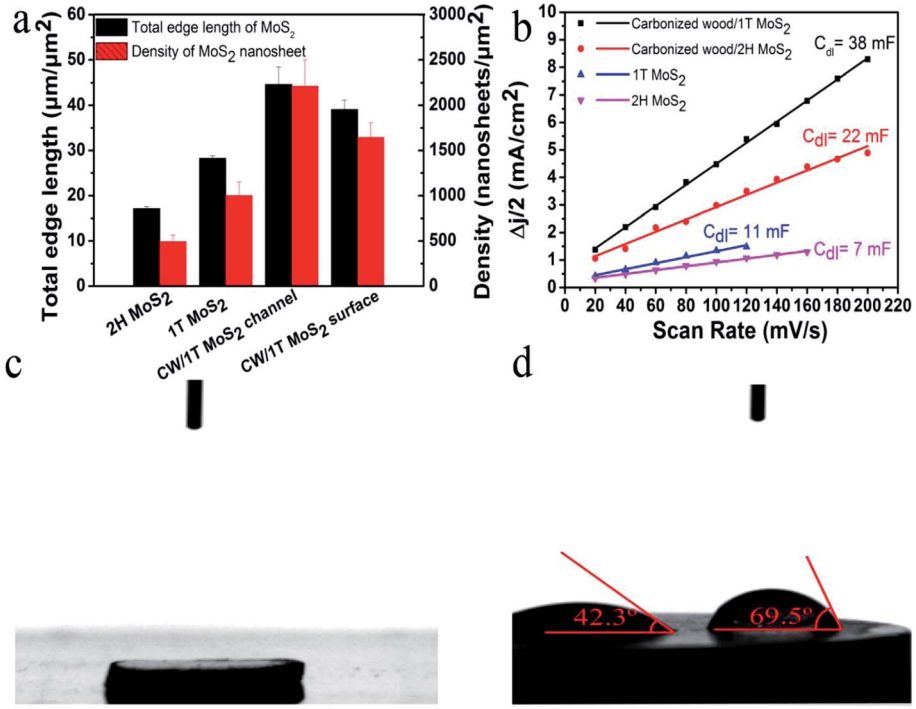

Fig. 6 (a) Statistical analysis of the total edge length and density of the MoS_2 nanosheets in a 1 μm^2 area. (b) The differences in the current density at 0.15 V *vs.* RHE plotted against the scan rate and fitted to a linear regression to estimate the C_{dl}. (c) The contact angle measurement data showing the wettability of CW/1T MoS_2. (d) The RDE coated with 1T MoS_2.

carbon surface after drying. However, 1T MoS_2 displays a structure resembling a nano-flower morphology (Fig. S7(b)†) with an abundance of active edges when compared to 2H MoS_2. The nanosheet structure of 1T MoS_2 formed a perfect array on the channel (Fig. S7(c)†) and the surface of the carbonized wood (Fig. S7(d)†). We further analyzed the total edge length of the MoS_2 nanosheets on glassy carbon and carbonized wood, as shown in Fig. 6(a). The total edge length of 2H MoS_2 and 1T MoS_2 coated on glassy carbon were 17.12 and 28.27 μm μm^{-2}, respectively, which are both significantly lower than the corresponding values of 44.62 and 39.10 μm μm^{-2} observed for their growth on the carbonized wood channel and surface, respectively. We also compared the number of MoS_2 nanosheets mounted on the different substrates. As shown in Fig. 6(a), when grown on the carbonized wood channels, the number of 1T MoS_2 nanosheets was 2212 nanosheets μm^{-2}, approximately 4.5 times higher than that of 2H MoS_2 coated on glassy carbon (492 nanosheets μm^{-2}). The number of nanosheets for 2H MoS_2 on the glassy carbon substrate was much lower than that of 1T MoS_2 on the same substrate (1002 nanosheets μm^{-2}). These results clearly demonstrate that the presence of carbonized wood encouraged the heterogeneous nucleation of 1T MoS_2 to form MoS_2 nanosheets vertically aligned to the surface of the carbonized wood.

Besides the active edge length, we further estimated the C_{dl} using cyclic voltammetry (CV). The results in Fig. 6(b) and S8† show that this was directly proportional to the effective electrochemical surface area.[35] The highest capacitance of ~38 mF, which is approximately 3.5 times higher than that found for pure 1T MoS_2 coated on glassy carbon (11 mF), was obtained for CW/1T MoS_2. The high value of C_{dl} can be attributed to the uniformity and vertical growth strategy of the MoS_2 nanosheets and the abundance of open channels that expose more accessible active sites. This occurrence is consistent with the estimation of the overall length and number of the active edges. In order to investigate the efficiency of the plasma treatment and the degree of wetting, the dynamic contact angle was measured on the surface of RDE coated with 1T MoS_2 and CW/1T MoS_2. The CW/1T MoS_2 was super hydrophilic exhibiting an initial contact angle of 0° (the theoretical lower limit of wettability) since the water droplet spreads on the surface instantly and turns into a flat puddle, as illustrated in Fig. 6(c) and ESI Video 3.† On the other hand, the RDE coated with 1T MoS_2 showed inferior wettability when compared to CW/1T MoS_2 with a contact angle of 42.3 and 69.5°, and the liquid formed a semi-compact sessile droplet on top of the disk electrode surface, as illustrated in Fig. 6(d) and ESI Video 4.† These results clearly indicate that the super hydrophilic properties of CW/1T MoS_2 increased the intensity of the phase contact between the liquid and the solid substances, and further accelerated the flow of electrolyte and the exhaustion of H_2.

Conclusions

In summary, inspired by nature, we have developed a highly efficient and freestanding working electrode for the production of H_2 using *in situ* vertically grown 1T MoS_2 nanosheets on well-aligned carbonized wood channels. There are two levels of

organizational alignments in the freestanding electrode: level one: the vertical alignment of nanosheets, which maximizes the exposure of active sites on the edge and basal planes of the 1T MoS_2. The C_{dl} of CW/1T MoS_2 is increased 3.5 times when compared to 1T MoS_2 deposited on glassy carbon, and level two: the perfectly aligned channels obtained from nature, which remarkably enhance electrolyte transport and H_2 dissipation. Furthermore, the carbonized wood exhibits super hydrophilicity after an anisotropic plasma treatment, which will benefit the contact between the electrode and electrolyte, and promote the release of the H_2 from the electrode surface. CW/1T MoS_2 enables a rapid HER with an overpotential of 128 mV *vs.* RHE at 10 mA cm^{-2}, which is significantly lower than that observed for pure 1T MoS_2 directly layered on a glassy carbon electrode (199 mV *vs.* RHE). Moreover, CW/1T MoS_2 was also electrochemically stable, which significantly reduced the frequency of refreshing the active catalyst. Thus, this approach towards synthesizing low cost, freestanding and highly efficient 1T MoS_2 on carbonized wood with well-aligned channels leads to an advancement of the HER reaction with highly competitive performance for large-scale hydrogen production.

Experimental

Preparation of CW/1T MoS_2

A piece of basswood (5 × 5 × 0.1 cm) was purchased from Walnut Hollow Company (Dodgeville, USA). The basswood pieces were pretreated at 240 °C for 4 h in air and carbonized at 1000 °C for 6 h in an argon environment to obtain the carbonized wood sample. 5.2 mg mL^{-1} of $Na_2MoO_4 \cdot 2H_2O$ (Sigma-Aldrich, USA) and 8.7 mg mL^{-1} of L-cysteine (Sigma-Aldrich, USA) were completely dissolved in DMF–H_2O solvent (v/v = 1.5 : 1) using a magnetic stirrer. The mixture was loaded into an autoclave (Parr Instrument Cop. USA), and the carbonized wood pieces were soaked in the mixture at 200 °C for 12 h. The CW/1T MoS_2 was repeatedly washed with DI water and dried at room temperature.

Plasma treatment

All plasma treatments were conducted using an Unaxis Plasma Therm 790 system and an RF power supply of 13.56 MHz used for the plasma excitation. During the oxygen plasma treatment, the system pressure and oxygen flow rate were kept constant at 2 mT and 25 sccm, respectively. The RF plasma power was 150 W and the exposure time was 15 s.

Scanning electron microscopy (SEM) observations

The morphology of the CW/1T MoS_2 was examined at an accelerating voltage of 2 kV using high-resolution SEM (Hitachi S4800, USA). Radial and longitudinal cross-sections of CW/1T MoS_2 were obtained by freeze fracturing the samples in liquid nitrogen.

High-resolution transmission electron microscopy (HRTEM)

HRTEM images were analyzed using an HRTEM JEOL 2010F (Tokyo, Japan) at an acceleration voltage of 200 kV. A sample, after milling and bath sonication (20 min), was dropped and dried onto holey carbon grids (Hatfield, USA). The SAED pattern of CW/1T MoS_2 was also recorded using HRTEM.

X-Ray diffraction (XRD)

The crystal structures of carbonized wood, 1T MoS_2 and CW/1T MoS_2 were investigated using XRD (PANalytical X'Pert Pro, Netherlands) equipped with Cu Kα radiation. The data was collected from 5° to 80° at a scan rate of 0.02° s^{-1}.

Raman spectroscopy

Raman spectroscopy was performed under 532 nm laser excitation using a LabRam HR800 UV NIR (Horiba Scientific, USA). The carbonized wood, 1T MoS_2 and CW/1T MoS_2 samples were measured by mounting them on a silicon substrate.

X-ray photoelectron spectroscopy (XPS)

The XPS spectra of carbonized wood, 1T MoS_2 and CW/1T MoS_2 were collected using a Thermo Scientific K-Alpha XPS (Waltham, USA) system equipped with a monochromatic aluminum Kα X-ray source (1486.6 eV). The pass energy and scan width were set at 50.0 eV and 0.1 eV, respectively.

Thermogravimetric analysis (TGA)

TGA was carried out to analyze the degradation properties of the carbonized wood, 1T MoS_2 and CW/1T MoS_2 samples using a TGA Q50 (TA Instruments, USA) apparatus. The samples were heated in the air at a heating rate of 10 °C min^{-1} in the temperature range from 40 to 700 °C.

Electrochemical measurements

The electrochemical measurements were performed using a classical three-electrode system on a biologic electrochemical station (SP-150). CW/1T MoS_2 (geometric area of 0.2 cm^2) was used as the working electrode, platinum foil as the counter electrode and the Ag/AgCl (in 3.5 M KCl solution) as the reference electrode in a 0.5 M H_2SO_4 solution. In all the measurements, the potential of the reference electrode was adjusted with respect to the RHE using the equation, $E_{(RHE)} = 0.059\ pH + E^{o}_{(Ag/AgCl)} + E_{(Ag/AgCl)}$, where the pH of the electrolytic solution was 0 and $E^{o}_{(Ag/AgCl)}$ was 0.270 V. 20 μL of the 2H MoS_2 and 1T MoS_2 suspensions (1 mg mL^{-1}) were dropped individually onto a 5 mm diameter glassy carbon disk electrode and air dried for 24 h. Linear sweep voltammetry was carried out at a scan rate of 2 mV s^{-1}. The electrochemical impedance circuit was considered to be a simplified Randles circuit to extract the series resistance and charge-transfer resistance. The electrochemical stability was calculated by continuously cycling 1000 times within a potential range from +0.1 V to −0.5 V *vs.* RHE. To estimate of the C_{dl} from the cyclic voltammograms (CV), the potential was swept at different scan rates (20, 40, 60, 80, 100, 120, 140, 160, 180 and 200 mV s^{-1}) within the potential range of 0.1–0.2 V *vs.* RHE.

Conflicts of interest

There are no conflicts to declare.

Acknowledgements

H. L. Zhu acknowledges the financial start-up support and Tier 1 support from Northeastern University. We would like to acknowledge the Center for Nanoscale Systems (CNS) at Harvard University for using their facilities. We also thank George J. Kostas Nanoscale Technology and Manufacturing Research Center at Northeastern University for the use of their XRD and plasma treatment instruments. Finally, we appreciate the support from Dr Marilyn L. Minus, Northeastern University for giving us the access to the TGA apparatus.

References

1 K. J. Jeon, H. R. Moon, A. M. Ruminski, B. Jiang, C. Kisielowski, R. Bardhan and J. J. Urban, *Nat. Mater.*, 2011, **10**, 286–290.
2 I. Tsuji, H. Kato and A. Kudo, *Angew. Chem.*, 2005, **117**, 3631–3634.
3 H. Wang, H. Yuan, S. S. Hong, Y. Li and Y. Cui, *Chem. Soc. Rev.*, 2015, **44**, 2664–2680.
4 J. X. Guo, F. F. Li, Y. F. Sun, X. Zhang and L. Tang, *J. Power Sources*, 2015, **291**, 195–200.
5 M. Fang, W. Gao, G. Dong, Z. Xia, S. Yip, Y. Qin, Y. Qu and J. C. Ho, *Nano Energy*, 2016, **27**, 247–254.
6 Z. Pu, Q. Liu, C. Tang, A. M. Asiri and X. Sun, *Nanoscale*, 2014, **6**, 11031–11034.
7 Y. Zhang, B. Ouyang, J. Xu, S. Chen, R. S. Rawat and H. J. Fan, *Adv. Energy Mater.*, 2016, **6**, 1600221.
8 H. B. Wu, B. Y. Xia, L. Yu, X. Y. Yu and X. W. D. Lou, *Nat. Commun.*, 2015, **6**, 6512.
9 J. Xie, H. Zhang, S. Li, R. Wang, X. Sun, M. Zhou, J. Zhou, X. W. D. Lou and Y. Xie, *Adv. Mater.*, 2013, **25**, 5807–5813.
10 K. Chang, X. Hai, H. Pang, H. Zhang, L. Shi, G. Liu, H. Liu, G. Zhao, M. Li and J. Ye, *Adv. Mater.*, 2016, **28**, 10033–10041.
11 Y. Yin, J. Han, Y. Zhang, X. Zhang, P. Xu, Q. Yuan, L. Samad, X. Wang, Y. Wang and Z. Zhang, *J. Am. Chem. Soc.*, 2016, **138**, 7965–7972.
12 X. Geng, W. Sun, W. Wu, B. Chen, A. Al-Hilo, M. Benamara, H. Zhu, F. Watanabe, J. Cui and T. P. Chen, *Nat. Commun.*, 2016, 7.
13 J. Guo, H. Zhu, Y. Sun, L. Tang and X. Zhang, *Electrochim. Acta*, 2016, **211**, 603–610.
14 X. Zhang, Q. Zhang, Y. Sun, P. Zhang, X. Gao, W. Zhang and J. Guo, *Electrochim. Acta*, 2016, **189**, 224–230.
15 D. Voiry, M. Salehi, R. Silva, T. Fujita, M. Chen, T. Asefa, V. B. Shenoy, G. Eda and M. Chhowalla, *Nano Lett.*, 2013, **13**, 6222–6227.
16 H. Li, C. Tsai, A. L. Koh, L. Cai, A. W. Contryman, A. H. Fragapane, J. Zhao, H. S. Han, H. C. Manoharan and F. Abild-Pedersen, *Nat. Mater.*, 2016, **15**, 48–53.
17 H. Zhu, F. Lyu, M. Du, M. Zhang, Q. Wang, J. Yao and B. Guo, *ACS Appl. Mater. Interfaces*, 2014, **6**, 22126–22137.
18 Y. Yan, B. Xia, N. Li, Z. Xu, A. Fisher and X. Wang, *J. Mater. Chem. A*, 2015, **3**, 131–135.
19 H. Wang, Z. Lu, D. Kong, J. Sun, T. M. Hymel and Y. Cui, *ACS Nano*, 2014, **8**, 4940–4947.
20 J. S. Li, Y. Wang, C. H. Liu, S. L. Li, Y. G. Wang, L. Z. Dong, Z. H. Dai, Y. F. Li and Y. Q. Lan, *Nat. Commun.*, 2016, **7**, 11204.
21 D. Kong, H. Wang, J. J. Cha, M. Pasta, K. J. Koski, J. Yao and Y. Cui, *Nano Lett.*, 2013, **13**, 1341–1347.
22 Y. Yang, H. Fei, G. Ruan, C. Xiang and J. M. Tour, *Adv. Mater.*, 2014, **26**, 8163–8168.
23 Z. Xiang, Z. Zhang, X. Xu, Q. Zhang and C. Yuan, *Carbon*, 2016, **98**, 84–89.
24 H. Vogt and K. Stephan, *Electrochim. Acta*, 2015, **155**, 348–356.
25 K. Zeng and D. Zhang, *Prog. Energy Combust. Sci.*, 2010, **36**, 307–326.
26 A. Liu, L. Zhao, J. Zhang, L. Lin and H. Wu, *ACS Appl. Mater. Interfaces*, 2016, **8**, 25210–25218.
27 W. Wei, K. Sun and Y. H. Hu, *J. Mater. Chem. A*, 2016, **4**, 12398–12401.
28 M. Wu, J. Zhan, K. Wu, Z. Li, B. Geng, L. Wang and D. Pan, *J. Mater. Chem. A*, 2017, **5**(27), 14061–14069.
29 Y. Sun, F. Alimohammadi, D. Zhang and G. Guo, *Nano Lett.*, 2017, **17**, 1963–1969.
30 S. Cadot, O. Renault, M. Frégnaux, D. Rouchon, E. Nolot, K. Szeto, C. Thieuleux, L. Veyre, H. Okuno and F. Martin, *Nanoscale*, 2017, **9**, 538–546.
31 J. Ekspong, T. Sharifi, A. Shchukarev, A. Klechikov, T. Wågberg and E. Gracia-Espino, *Adv. Funct. Mater.*, 2016, **26**, 6766–6776.
32 T. Wang, G. Zhao, C. Sun, L. Zhang, Y. Wu, X. Hao and Y. Shao, *Adv. Mater. Interfaces*, 2017, **4**(14), 1601187.
33 K. Zhang, Y. Zhao, S. Zhang, H. Yu, Y. Chen, P. Gao and C. Zhu, *J. Mater. Chem. A*, 2014, **2**, 18715–18719.
34 H. Yu, X. Yu, Y. Chen, S. Zhang, P. Gao and C. Li, *Nanoscale*, 2015, **7**, 8731–8738.
35 M. A. Lukowski, A. S. Daniel, F. Meng, A. Forticaux, L. Li and S. Jin, *J. Am. Chem. Soc.*, 2013, **135**, 10274–10277.